

## JGR Solid Earth

## RESEARCH ARTICLE

10.1029/2019JB017494

## Key Points:

- Since 1980, three prolific natural earthquake swarms occurred between the Elsinore and San Jacinto faults, in the central Peninsular Ranges
- These swarms are driven by interseismic plate boundary strain rates and modulated by pore fluid pressure in low-permeability plutonic rock
- Shallow depths, absence of mapped faults, and nonlinear seismic moment release suggest concurrent slip on foliations in the plutonic rock

## Correspondence to:

E. Hauksson,  
hauksson@caltech.edu

## Citation:

Hauksson, E., Ross, Z. E., & Cochran, E. (2019). Slow-growing and extended-duration seismicity swarms: Reactivating joints or foliations in the Cahuilla Valley pluton, central Peninsular Ranges, Southern California. *Journal of Geophysical Research: Solid Earth*, 124, 3933–3949. <https://doi.org/10.1029/2019JB017494>

Received 2 FEB 2019

Accepted 24 MAR 2019

Accepted article online 28 MAR 2019

Published online 15 APR 2019

## Slow-Growing and Extended-Duration Seismicity Swarms: Reactivating Joints or Foliations in the Cahuilla Valley Pluton, Central Peninsular Ranges, Southern California

Egill Hauksson<sup>1</sup> , Zachary E. Ross<sup>1</sup> , and Elizabeth Cochran<sup>2</sup> 

<sup>1</sup>Seismological Laboratory, Division of Geological and Planetary Sciences, California Institute of Technology, Pasadena, CA, USA, <sup>2</sup>Earthquake Science Center, U.S. Geological Survey, Pasadena, CA, USA

**Abstract** Three prolific earthquake swarms and numerous smaller ones have occurred since 1980 in the Mesozoic igneous plutonic rocks of the Perris block of the Peninsular Ranges, Southern California. The major swarms occurred in 1980–1981, 1983–1984, and 2016–2018, with the latest swarm still ongoing. These swarms have no clear mainshock, with the largest events of  $M_L$  3.6,  $M_L$  3.7, and  $M_w$  4.4. Each successive swarm had larger cumulative seismic moment release with about 314 and 411 events of  $M \geq 1.5$ , while the third swarm has produced about 451 events of  $M \geq 1.5$  (as of September 2018). The concurrent strike-slip faulting occurred on north to northwest striking planes but with no orthogonal northeast trending seismicity alignments. These shallow swarms are probably driven by intrablock Pacific-North America plate boundary stress loading of the two bounding major late Quaternary strike-slip faults, the Elsinore and San Jacinto faults. The state of stress within the Cahuilla Valley pluton has a  $\sim 40^\circ$  angle between the maximum principal stress and the average trend of the swarms, suggesting that migrating pore fluid pressures aid in the formation and growth of zones of weakness. These swarms, which last more than 600 days each, exhibit clear bilateral spatial migration for distances of up to  $\sim 7$ – $8$  km and reach their full length in about 20 months. The slow spatial-temporal development of the swarms corresponds to a fluid diffusivity of 0.006 to 0.01  $\text{m}^2/\text{s}$ , consistent with very low permeability rocks as expected for this block. There is no geodetic or other evidence for a slow slip event driving the swarms.

**Plain Language Summary** There have been three unusual seismicity swarms in the Cahuilla Valley, Peninsular Ranges, over the last 40 years: 1980–1981, 1983–1984, and 2016–2018, with the latest still ongoing. They occurred within granite rocks that underlie the Cahuilla Valley pluton. The first two lasted for about 2 years, and the current swarm is still ongoing more than 2.5 years after it began. These swarms differ from mainshock-aftershock sequences because the largest events occur months after the swarm initiation event. These swarms are probably driven by plate boundary stress loading of the two bounding major late Quaternary strike-slip faults, the Elsinore and San Jacinto faults, and aided by changes in pore fluid pressures.

### 1. Introduction

Southern California seismicity is mostly caused by Pacific and North America relative plate motion that is accommodated along major crustal-scale late Quaternary faults (Hutton et al., 2010). Other processes such as gravitational collapse of mountain ranges, crustal delamination, natural or induced fluid flow, and geothermal activity also cause seismicity (Hauksson et al., 2012). Seismicity occurs mostly as mainshock-aftershock sequences, but swarms are more common in transtensional regions, including the Salton Trough and eastern California, as well as geothermal areas (e.g., Vidale & Shearer, 2006; Zaliapin & Ben-Zion, 2013).

In addition, there are less well-understood swarms that occur within batholiths in the western United States, away from the late Quaternary faults. In this study, we analyze such swarms within the Perris block of the northern Peninsular Ranges. The Perris block forms the eastern part of the Peninsular Ranges and is characterized by continental margin magmatic arc rocks of tonalite composition (Morton et al., 2014). In contrast to typical swarm areas in Southern California, the Perris block is mostly aseismic, has low heat flow, and has low tectonic strain rate. There is also noticeable absence of late Quaternary faults within the dense, low-porosity, and low-permeability plutonic rocks (Morton et al., 2014).

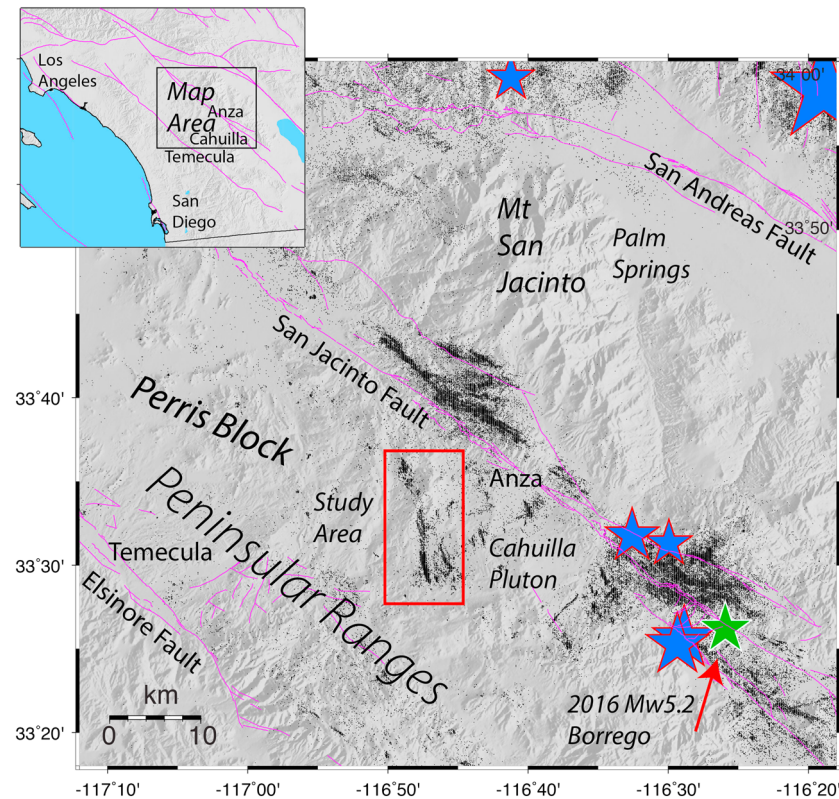


**Figure 1.** Map showing the location of the study area and regional seismicity (~113,000 events) from 1981 to September 2018. Major late Quaternary faults from Jennings and Bryant (2010) are shown in magenta. Earthquakes of  $M \geq 5.0$  are shown as stars with red outlines and solid blue color. The red box outlines the study area. The red arrow points to the green star with a white outline that represents the 2016  $M_w$  5.2 Borrego earthquake.

There have been three major seismicity swarms in the Cahuilla Valley over the last 40 years: 1980–1981, 1983–1984, and 2016–2018, with the latest still ongoing. Note that although the latest swarm is ongoing, we label this the 2016–2018 swarm since that is the date range of available data used in this study. These swarms are unusual in several respects (Figure 1). First, they occurred within the Mesozoic pluton in the Perris block, away from any mapped late Quaternary faults, about midway between the Elsinore and San Jacinto faults (Morton et al., 2014). Second, the first two lasted for about 2 years, which is unusually long for Southern California swarms, and the current swarm is still ongoing more than 2.5 years after it began. Third, the largest events in each swarm occur months after the swarm initiation event. The amount of seismic moment release in these swarms is small, corresponding to a fraction of a  $M$  5 earthquake, which would have a shorter fault length of ~1 to 2 km as compared to the longest dimension of these swarms (~5 km; Wells & Coppersmith, 1994). Fourth, the abundance of small earthquakes suggests the presence of a balance between moment release and stress loading that causes a large number of small events.

Similar shallow earthquake swarms are common within other batholithic terranes in the western United States. Vidale and Shearer (2006) identified several short-time-length (less than 28 days) swarms in the southern Sierra Nevada. Ruhl et al. (2016) described the 2008  $M_w$  4.9 Mogul swarm that occurred within the Sierra batholith, near Reno Nevada. The overall length was ~15 km, and the depth extent was similar to the Cahuilla swarms or ~6 km. The overall fault structure was a dominant right-lateral northwest trend with minor left-lateral orthogonal faults. Another example was the 2017 Sulphur Peak, Idaho, mainshock of  $M_w$  5.3, which was followed by an extended (lasting for a few months) unusual swarm-like aftershock sequence, which was attributed to slow aseismic slip (Koper et al., 2018).

We analyze seismicity data from the three Cahuilla swarms that are aligned almost north-south, possibly along geologically defined lineations. We compare the spatial-temporal evolution and seismic properties

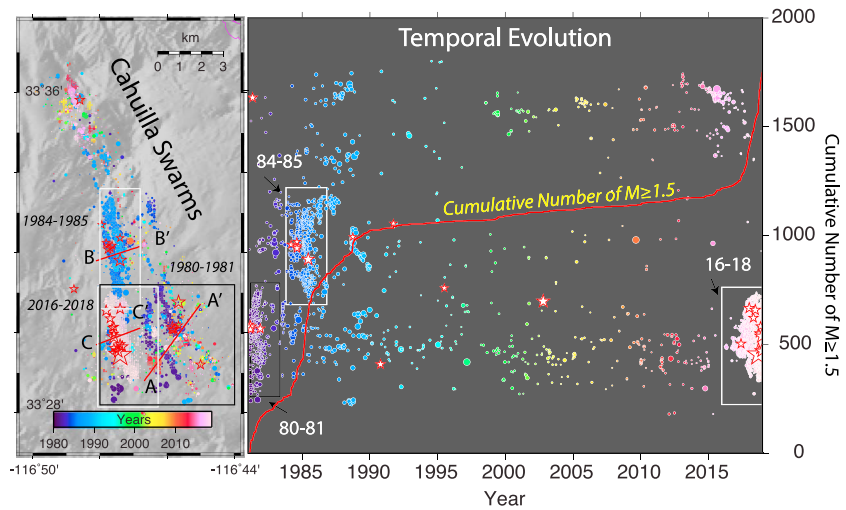


**Figure 2.** (left) Map showing the locations of the three swarms with locations of cross sections (A, B, and C red lines) shown in Figure 4. (right) Latitude versus date (year) showing the temporal evolution of the seismicity with events of  $M < 3.0$  as circles and 23 events of  $M \geq 3.0$  as stars. The cumulative number of 1,696 events of  $M \geq 1.5$  recorded from 1980 to 2018 is shown as a red curve with a scale on the right-hand side as vertical axis. In both figures, the approximate outlines of the swarms are shown as white or black boxes, and all events are color coded by date.

of these swarms to infer the possible driving mechanisms (Figure 2). We also compare their temporal behavior with the nearby 2016  $M_w$  5.2 Borrego Springs mainshock-aftershock sequence (Ross et al., 2017). The Borrego sequence was selected because it is the best recorded nearby mainshock-aftershock sequence. Our goal is to understand the temporal evolution and seismic moment release in these swarms, even though the temporal behavior is rich with embedded aftershock sequences.

## 2. Data Processing

For our data analysis we used the updated relocated Southern California Seismic Network (SCSN) catalog that was developed with the approach of Hauksson et al. (2012). All of the Cahuilla events were detected by the SCSN automated picker and reviewed by data analysts. The relocation process consists of the following three steps: (1) We first locate the events using a Southern California 1-D velocity model; (2) we relocate the events individually by applying a 3-D velocity model (Hauksson, 2000); and (3) we determined relative arrival times via cross correlation to 750 nearest neighbors, and we used the clustering algorithm from Matoza et al. (2013) to perform a pairwise double-difference relocation of the events. We relocated the 1980 seismicity using the 3-D velocity model but without waveform cross correlations. The waveforms for the events that occurred in 1980 are of low quality and have not been cross-correlated. In some of the figures we also included the 1980 seismicity from the SCSN catalog, to display the beginning of the 1980–1981 swarm.

We list in Table 1 the first event in each swarm, which we use as the initiation point for the diffusivity estimates. These events were selected because they appear to be the initiation point for the whole swarm. Another nearby event in time or space could have been picked, but these events best match the fit of the

**Table 1**  
*The Initial Event in Each Swarm*

Date	GMT	Latitude	Longitude	Depth (km)	Event ID #
1 Jan 1981	06 hr 17 m	33° 29.51'	−116° 47.15'	5.5	3301498
5 Apr 1984	10 hr 39 m	33° 32.34'	−116° 47.41'	4.7	35902
11 Sep 2016	19 hr 19 m	33° 29.65'	−116° 47.31'	6.5	37475951

diffusivity curves to the seismicity space-time distribution. There is a short gap in the catalog in March 1981 due to technical difficulties in SCSN operations. Other gaps are considered to be real.

Small events are easily detected in this region, because of the good SCSN monitoring coverage, low background seismic noise levels, and the high near-surface  $Q$  values for the plutonic rocks (Hauksson & Shearer, 2006). Improvements in SCSN data quality since 1980 affect the magnitude of completeness ( $M_c$ ) as well as focal depth distributions. The availability of  $P$  and  $S$  picks to determine the hypocenters varies through time, and correspondingly, the errors become smaller when more short-distance picks are available. For the 2016–2018 swarm the one-sigma errors for horizontal accuracy range from 0.1 to 0.6 km with a mean error of 0.25 km. Similarly, the vertical errors range from 0.2 to 1.0 km with a mean vertical error of 0.6. These errors are small because one of the seismic stations (NP.5241) is located with 1.0 to 4.0 km of the majority of the events. Similarly, the average horizontal and vertical errors for the 1984–1985 swarm range from 0.3 to 0.7 km. The average vertical errors for the 1980–1981 swarm are larger or about 2.5 km because the nearest station was located about 18 km away, but the vertical errors became smaller when a station was installed about 5 km away in June 1981. Usually, the relative errors are an order of magnitude smaller than the absolute errors (Hauksson et al., 2012).

We used the Yang et al. (2012) approach to measure  $S/P$  amplitudes and the HASH method of Hardebeck and Shearer (2003) for determining focal mechanisms using both first motions and  $S/P$  amplitudes. The events analyzed for this study are of A, B, and C quality, with average angular uncertainty of  $\sim 30^\circ$ . We applied the method of Michael (1984) to invert the focal mechanism data for the orientations of the principal stresses and the corresponding stress ratio for each swarm. We calculated maximum likelihood  $b$  values using ZMAP software (Wiemer, 2001).

### 3. Results

The Cahuilla swarms were located 10 to 20 km away from two major Pacific-North America plate boundary faults, the Elsinore and San Jacinto faults, which strike to the northwest across the region. We focus our analysis on the three swarms (1980–1981, 1983–1984, and 2016–2018, which we also use as names for the swarms) as outlined by the black box and two white boxes (Figure 2). We compare various features of the three swarms including spatial and temporal evolution, focal mechanisms and stress, temporal evolution of the seismicity rate, Gutenberg-Richter distributions, interevent time distributions, and cumulative seismic moment release. In turn, we interpret the characteristics of the swarms to estimate hydraulic diffusivity and fluid pore pressures.

#### 3.1. Spatial and Temporal Evolution

The three swarms had spatial extents of  $\sim 5$  to  $\sim 7$  km and lasted for  $\sim 2$  to over 2.5 years. The first two swarms were separated in time by about  $\sim 2$  years, while the third swarm occurred  $\sim 31$  years later. Low-level background seismicity in the intervening period (1985–2016) was more prevalent in the southern part of the study region near the first swarm. The minimum  $M_c$  of the SCSN catalog for this region was  $\sim 1.5$  until about a decade ago, with a  $M_c \sim 0.5$  for the most recent swarm (Figure 2).

The 1980–1981 Cahuilla swarm consisted of several tight clusters spatially distributed over an area that extended  $\sim 3$  km in the east-west direction and  $\sim 5$  km to the north-south, across the western Cahuilla Valley proper (Figure 2). The swarm started in June 1980 with a relatively low seismicity rate and grew bilaterally north-south for  $\sim 2$  years (Figure 3). In February 1981 a  $M_L$  3.6 earthquake occurred, which was followed by a short-lived aftershock sequence. Background swarm activity continued for another year after this largest event.

The 1984–1985 Cahuilla swarm was located directly northwest of the 1980–1981 swarm. It started gradually in early February 1984 (Figure 3), followed by a  $M_L$  3.6 mainshock-aftershock sequence that occurred 3 months later. The aftershock sequence lasted for a few days and extended north-south  $\sim 2$  km. Elevated seismicity rate consisting of clusters of smaller events extended bilaterally away from the selected initial event for each swarm. After  $\sim 2$  years of activity, the swarm had formed a north-south lineation  $\sim 7$  km long.

The 2016–2018 Cahuilla swarm started in mid-2016, spatially overlapped the western third of the 1980–1981 swarm, and abutted the southern end of the 1984–1985 swarm. This Cahuilla swarm had a low level of

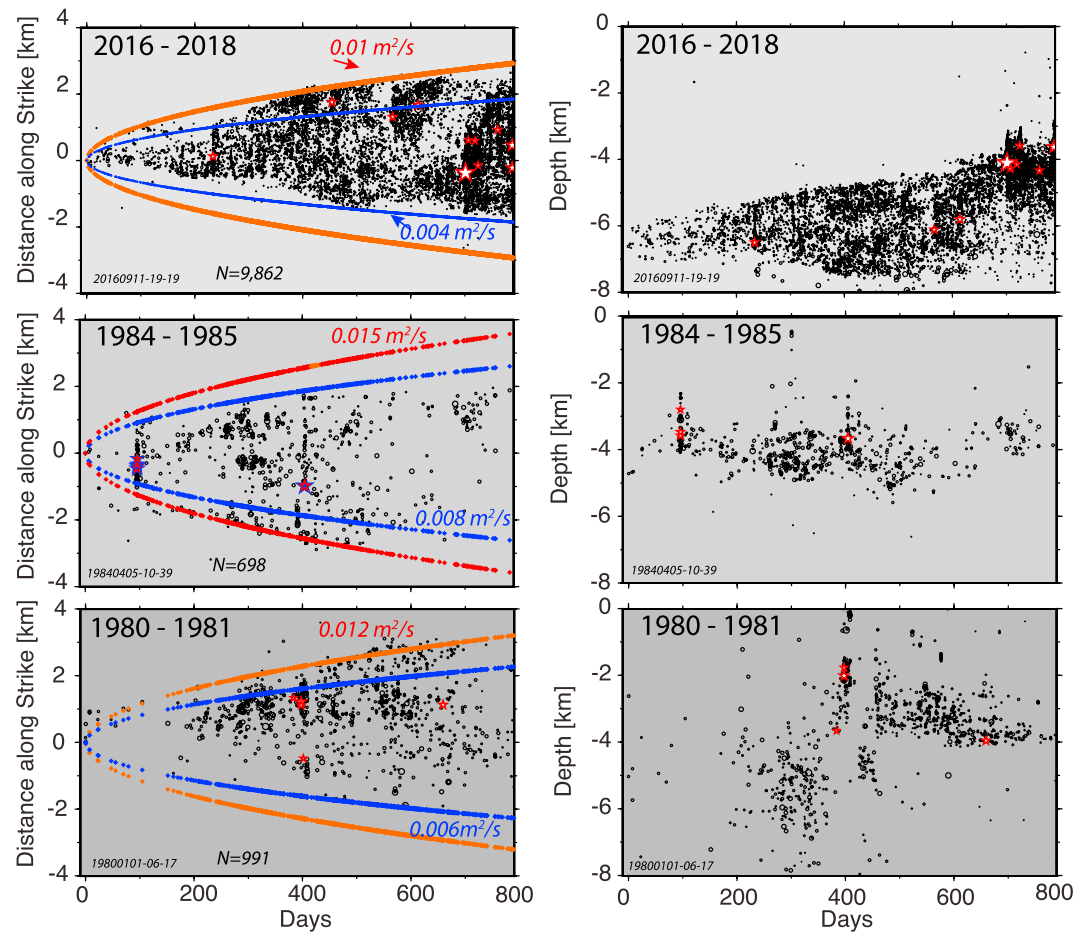


**Figure 3.** (left column) All located events in each swarm are plotted with distance along strike from the initial event in each swarm (Table 1) versus days. The  $N$  value is the number of recorded events in each swarm, and  $M \geq 3.0$  events are shown as red stars. The red and blue curves show the maximum and minimum diffusivity, respectively, calculated using the method of Shapiro et al. (1997). (right column) Focal depths versus date for all recorded events in the three clusters. The most recent cluster (2016–2018) includes more events because of the lower detection threshold and magnitude of completeness of  $M_c \sim 0.5$ .

activity at first but has grown steadily in number of events ( $\sim 7,300$  of  $M > 0.5$  as of 31 December 2018). It forms an almost north-south striking linear trend of  $\sim 5$  km (Figure 3). On 11 August 2018 the seismicity accelerated with an  $\sim 120$ -event foreshock sequence, which culminated with a mainshock of  $M_w$  4.4 on 15 August 2018. The  $M_w$  4.4 shock was followed by more than 143 aftershocks of  $M > 0.5$  over a period of 12 hr, and the overall rate of  $M \geq 1.5$  events increased by 2.5 over the following 4 months. This new activity extended the spatial distribution of the sequence  $\sim 0.2$  km to the south-southwest.

The focal depths relative to the sea level of each swarm exhibit different temporal depth distributions. These changes in the focal depth distributions also reflect improvements in the quality of focal depths with time (Figure 3). The 1980–1981 swarm consisted of events with scattered focal depth distribution reaching from  $\sim 0$ -km depths to  $\sim 8$  km, while the 1984–1985 swarm is limited to the depth range of  $\sim 2$  to  $\sim 5$  km. The 2016–2018 swarm, which has the best determined focal depths with uncertainties of  $< 1$  km, exhibits upward and downward migrations in the depth range of 3 to 8 km, with the most recent focal depths at  $\sim 3$ - to  $\sim 6$ -km depth.

In general, these swarms are shallower than events along the San Jacinto or Elsinore faults, reaching only about half the depth of the  $\sim 14$ -km-thick seismogenic zone (Hauksson & Meier, 2018; Ross et al., 2017). In addition, the absence of clear geodetic (Global Navigation Satellite Systems (GNSS) and interferometric synthetic aperture radar) anomalies associated with the 2016–2018 swarm (Y. Fialko, personal

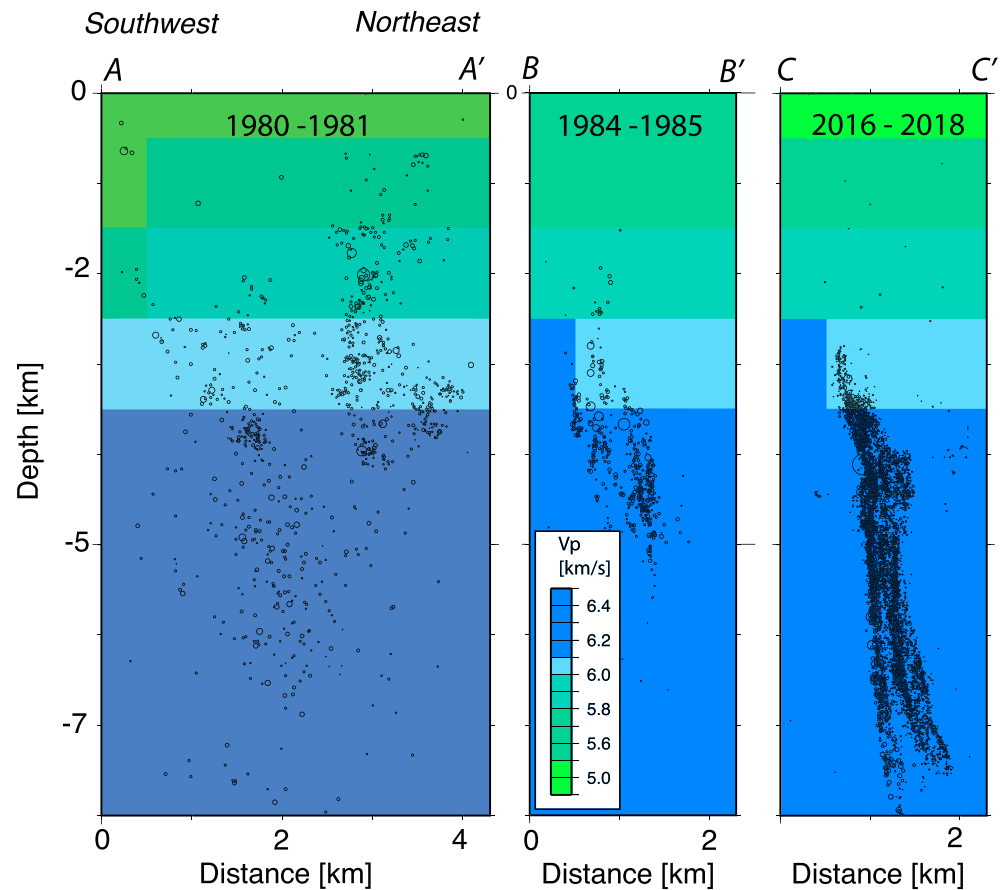


**Figure 4.** The southwest to northeast trending depth cross sections for the 1980–1981, 1984–1985, and 2016–2018 swarms are shown at the same scale. Only the seismicity in each swarm is included in the respective cross section as indicated in Figure 2. The background colors indicate the 3-D  $V_p$  model from Hauksson (2000). The map in Figure 2 shows the epicenters of the three swarms and locations of the cross sections as red lines.

communication, 19 April, 2018) is consistent with this swarm being of very limited spatial extent and occurring at shallow depths, given the large spacing (~30 km) between GNSS in the region.

We compare the depth distribution of the three swarms in Figure 4. All three swarms appear to illuminate several subparallel seismicity surfaces. In each swarm, the deformation occurred in a zone that is ~2 to ~4 km wide and ~5 to ~7 km long. Because the SCSN monitoring capabilities have improved over time, the focal depths of the 1980–1981 events are less well constrained than are the focal depths for the 1984–1985 and 2016–2018 swarms. This may explain the large depth scatter in the first swarm, but the overall relative shifts in the median of the depths by 1- or 2-km depths are well constrained by the pairwise double-difference relocation.

### 3.2. Focal Mechanisms and Stress

The focal mechanisms exhibit predominantly strike-slip motion with one of the nodal planes striking north to northwest, while the other strikes east to northeast, consistent with the regional stress loading (Lindsey & Fialko, 2013). The north to northwest striking nodal planes follow the general spatial trend of each swarm (Figure 5); note that there are no northeast to east cross-trending seismicity alignments. Motion along north to northwest striking planes is consistent with geological mapping of the region, which shows geomorphic lineaments in the area have a north to northwest strike (Morton et al., 2014).

In detail, the three swarms form several separate seismicity trends (Figure 4), suggesting that the seismic moment release is taking place on several subparallel fault strands. Such fault strands appear to show ~1-km separation in the 1980–1981 swarm, 0.5-km separation in the 1983–1984 swarm, and ~0.25-km separation in the 2016–2018 swarm. In addition, during the 2016–2018 swarm both the seismicity

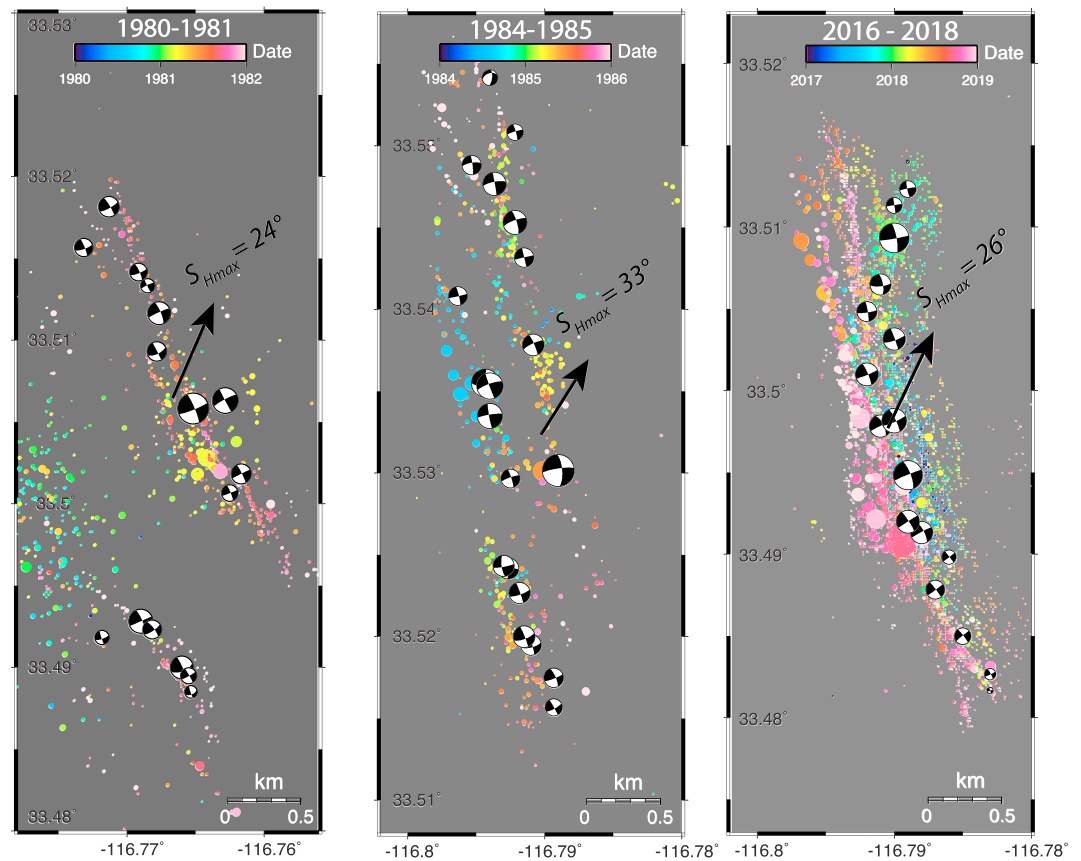


**Figure 5.** High-resolution maps of the three swarms showing color-coded epicenters with date, and randomly selected focal mechanisms. The map of the 2016–2018 swarm only includes events for  $M_c \geq 0.5$  for clarity. The black arrows indicate the azimuth of the  $S_{Hmax}$  direction as determined with stress inversion for each swarm (Michael, 1984).

trends and the nodal planes exhibit an apparent rotation in strike toward a more northerly orientation at the north end of the sequence.

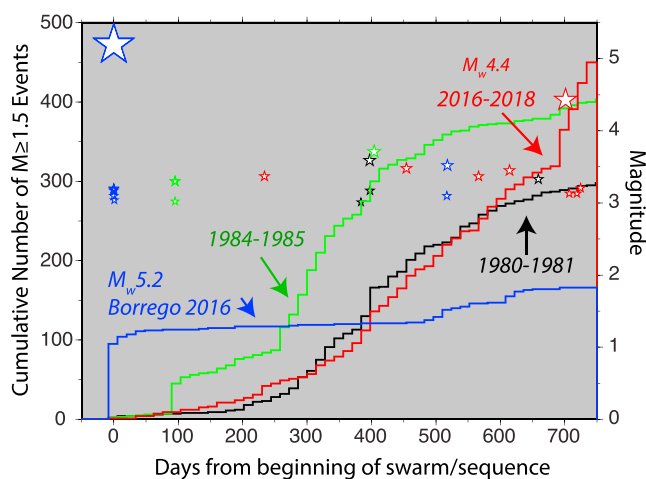


**Figure 6.** Cumulative number of  $M \geq 1.5$  events versus date for the three swarms and the 2016  $M_w$  5.2 Borrego sequence. Each cumulative distribution is plotted in a separate color (see labels) with corresponding events of  $M \geq 3.0$  events plotted as color-coded stars.

The azimuth of the horizontal component of the maximum principal stress ( $S_{Hmax}$ ) for the three swarms was determined by inverting for the state of stress for each swarm as  $24^\circ$ ,  $33^\circ$ , and  $26^\circ$  (Figure 5). The stress shape, defined as the ratio of  $(\sigma_1 - \sigma_2)$  to  $(\sigma_1 - \sigma_3)$  for all three swarms, is  $\sim 0.5$ , consistent with strike-slip faulting. These  $S_{Hmax}$  azimuth values are similar to the Southern California crustal stress field determined by Yang and Hauksson (2013).

### 3.3. Statistical Properties of the Swarms

The overall statistical properties such as rate of seismicity,  $b$  value, interevent time distribution, and seismic moment release of the three swarms are similar, but the details differ.

#### 3.3.1. Temporal Evolution of the Seismicity Rate

The beginning of the first two swarms had no clear mainshocks, here defined as being  $\sim 1.5$  magnitude units larger than other events in the swarm (Båth's law; Båth, 1965), with the largest events of  $M_L$  3.6 and  $M_L$  3.7 occurring months after the swarm initiated (Figure 6). The 2016–2018 swarm is strikingly similar in seismicity rate to the 1980–1981 sequence (until the last few months of 2018) and less prolific than the 1984–1985 swarm (again until the last few months of 2018 when a  $M_w$  4.4 event occurred) when comparing catalogs with similar  $M_c$  (Figure 6).

The temporal evolution of the seismicity rate in the three major swarms exhibited slow onset, lasting for ~100 to ~300 days (Figure 6). The 1980–1981 sequence seems to have a quite clear change in seismicity rate after ~200 days. The 1984–1985 sequence has a significant jump in the seismicity around 100 days and an overall higher rate after that sequence (that again increases ~250 days into the sequence). And the 2016–2018 swarm seems to have a steadily increasing rate, so it is difficult to define a slope break, but the rate changes near ~250–300 days. This slow onset is consistent with the absence of a step-function type load (e.g., a mainshock) that would have imparted a sudden stress pulse on the source region (Shapiro et al., 1997). This onset of all three swarms was followed by a steady rate of activity with ~25 events per month of  $M \geq 1.5$  for a duration of about 300 days. The steady seismicity rate suggests the presence of a persistent balance between loading, pore pressure, and stress release in the swarm regions. In comparison, the 2016  $M_w$  5.2 Borrego mainshock imparted an abrupt step-function load that caused a flurry of aftershocks within days, but the activity almost ceased during the following weeks to months.

### 3.3.2. Gutenberg-Richter Distributions

The Gutenberg-Richter distribution for the catalog of all three swarms has an average  $b$  value of ~0.9, which is similar to the average  $b$  value for Southern California (Hutton et al., 2010). We used an average completeness magnitude,  $M_c = 1.5$ , although the  $M_c$  varies for the three swarms, with  $M_c \sim 1.5$  for the first two swarms and  $M_c \sim 0.5$  for the most recent swarm.

The temporal and depth variations of  $b$  value are shown in Figure 7. Although the seismicity rate of each swarm fluctuates from day to day or week to week, the temporal changes in  $b$  value are small and within error bounds.

The  $b$  values with depth for the three swarms increase in the ~2- to ~4-km depth range for the 1980–1981 swarm, but the increase is deeper or ~3 to 5 km for the 1985–1985 and 2016–2018 swarms. This increase is most clearly observed in  $b$  value estimates for the 2016–2018 swarm; however, the overall increase is small or from  $\sim 0.9 + 0.02$  to  $\sim 1.3 \pm 0.08$ . The depth variations in  $b$  values suggest that the bulk of each swarm is occurring within a depth-limited weak zone as compared to the strength of the crustal blocks above and below.

### 3.3.3. Interevent Time Distributions

Interevent time distributions (sometimes called waiting time between successive events) depict the temporal occurrence of events within a swarm (Hainzl & Fischer, 2002; Touati et al., 2009). In other words, this is a way to describe temporal behavior (even if Omori's law does not hold) where there is no mainshock near the start of the sequence. The normalized density of number of  $M \geq 1.5$  events per day for detecting a waiting time  $W^{-w}$  between events for the 2016 Borrego sequence and the three Cahuilla swarms is shown in Figure 8. Logarithmically binned data from each sequence can be fit by a power law, which suggests that these swarms are strongly clustered in time. If these distributions were Poissonian in time, an exponential fit would provide a much better match (Hainzl & Fischer, 2002).

The interevent time distributions are correlated to the relative number of mainshocks in a catalog (Hainzl et al., 2006). The power law form of the interevent time distributions shows that the clustering properties of aftershock sequences and swarms are different from each other, with slower decay for extended-duration swarms. These swarms have stronger event correlations that appear as longer-duration distribution of interevent times. Because the swarms decay at a slower rate than an equivalent aftershock sequence, of similar moment release, the interevent time probability density functions provide a quantitative comparison of the clustering strength of seismicity sequences.

Hainzl (2004) showed that a power law description of an interevent time distribution of  $W^{-1.5}$  is clustered on all timescales (also referred to as fractal). We observe a fractal clustering for the 2016  $M_w$  5.2 Borrego aftershock sequence that decayed quickly (Figure 8). In contrast, the three swarms examined here exhibit lower power law decay, with the 1980–1981 and 1983–1984 swarms both having interevent time distributions of  $(W^{-0.9})$  and the 2016–2018 swarm having  $W^{-1.1}$ . The difference between the early two swarms and the more recent swarm reflects the relative role of mainshocks in the overall seismic moment release for each swarm (Hainzl et al., 2006). In general, these power law exponents for the swarms reflect the overall longer temporal duration of the swarms as compared to the 2016 Borrego earthquake aftershock zone.

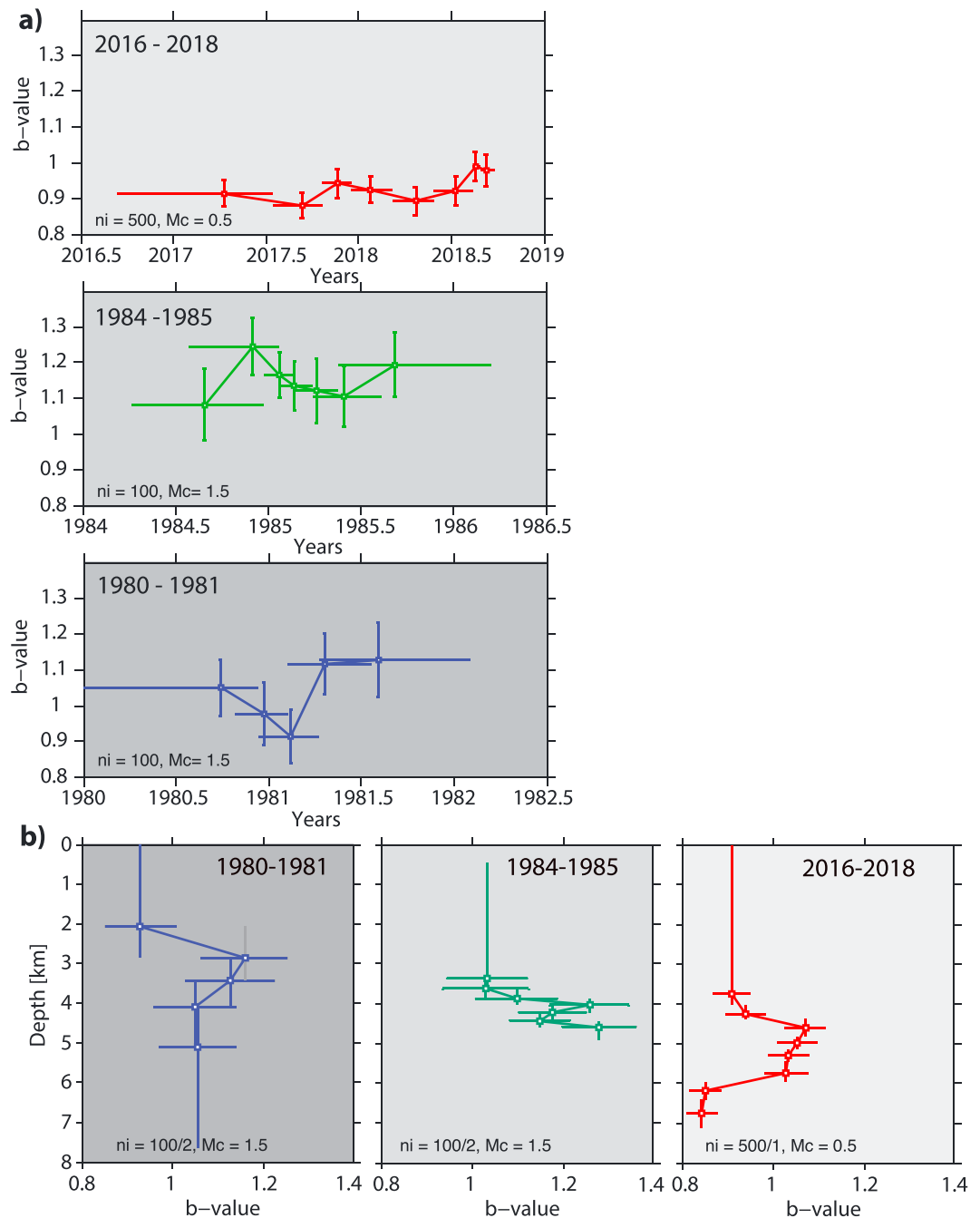


**Figure 7.** The maximum likelihood  $b$  values for the three Cahuilla swarms. (a)  $b$  values with date and (b)  $b$  values with depth. The number of events and overlaps ( $ni/x$ ) used in each  $b$  value calculation;  $x$  is the number of overlaps in depth plots.  $Mc$  values are shown in each panel.

### 3.3.4. Cumulative Seismic Moment Release

The cumulative seismic moment release as a function of earthquake number through time (event index) can be interpreted as diagnostic of the area that is involved in the overall rupture process when assuming constant plate tectonic loading rate (Hainzl & Fischer, 2002). In the special case where the area of seismic moment release does not significantly change across the time span of a sequence, and the stress loading rate is approximately constant, the cumulative moment rate is expected to be time independent, which would correspond to a slope of  $t^{1.0}$  in Figure 9.

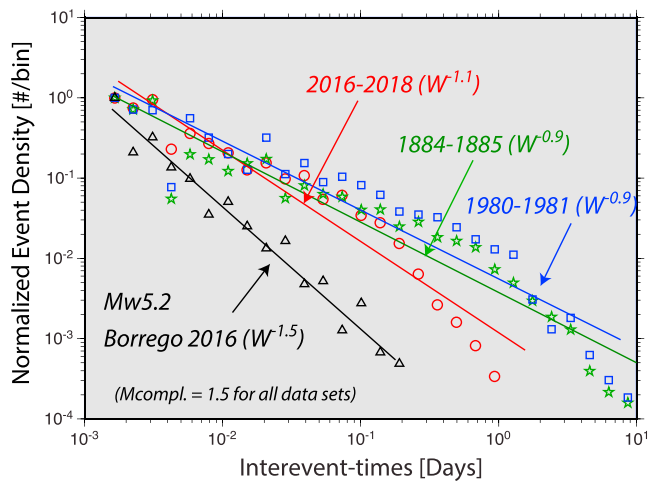


**Figure 8.** Probability density of number of  $M \geq 1.5$  events per day for detecting an interevent time  $W$  between events, for the 2016 Borrego sequence and the three Cahuilla swarms. Using logarithmic binning, data from each sequence can be fit by a power law that quantifies the temporal clustering of each sequence.

We examine the cumulative seismic moment release versus event index for the Cahuilla swarms and the 2016 Borrego sequence (Figure 9). The Borrego foreshocks and the 1984–1985 sequence show similar time-independent moment release behavior ( $i^{1.0}$ ). However, following the mainshock, the 2016 Borrego sequence moment release behavior changes abruptly. The moment release in the 1980–1981 and 2016–2018 swarms followed a steeper power law ( $i^{1.7}$ ), indicating larger than linear moment release per event.

Previously, Hainzl (2004) showed that this relationship ( $M_0 \sim i^{1/4}$ ) was consistent with basic fracture mechanics of a crack model. In a crack model the stress at the crack tip is proportional to the square root of crack extension parameter,  $c$ , which in turn is proportional to the square root of the crack area. For the 1980–1981 and 2016–2018 swarms, the  $i^{0.7}$  (where we have removed the linear part [ $i^{1.0}$ ]) suggests about 3 times higher moment release rate than observed by Hainzl and Fischer (2002) for the Vogtland swarms, located on the border region of Czech Republic and Germany.

The Vogtland swarms were interpreted to involve seismicity on a single rupture surface; thus, our results suggest that there may be several subparallel joints or slip surfaces accommodating the moment release in these

two Cahuilla swarms. This interpretation is also consistent with the three separate subparallel depth strands that were observed for the 2016–2018 swarm.

Stress drops for some of the Cahuilla events that were determined by Shearer et al. (2006) and by T. Goebel (personal communication, April 1, 2015) confirm that the slip surfaces are of average size as compared to other similar-sized events in Southern California. In general, they show typical Southern California values ranging from 0.1 to 10 (MPa), with a median of  $\sim 1.5$  (MPa). Thus, the stress drop values also support the idea of the presence of subparallel slip surfaces.

### 3.4. Hydraulic Diffusivity

Hydraulic diffusivity is the ratio that describes the balance between transport and storage of fluids in a rock (Song & Renner, 2007). In general, the diffusivity is controlled by permeability, fluid pore compressibility of the host rock material, and the fluid viscosity (Wibberley, 2002). The clear spatial-temporal migration, lack of mainshocks, and abundance of small events are consistent with pore fluids playing a major role in the evolution of Southern California swarms (Vidale & Shearer, 2006). We model the overall fluid-driven evolution of these three swarms using a 1-D fluid diffusion model (Malagnini et al., 2012; Shapiro et al., 1997). This model assumes that the earthquakes are triggered when the pressure front arrives at their hypocenter, although the peak stress may arrive somewhat later.

To determine the north and south diffusivity constants for each swarm, we select a first event and assign two envelope curves to each distribution (Table 1). We use the Shapiro et al. (1997) formula for the envelope:  $r = \sqrt{(4\pi Dt)}$  where  $r$  is distance,  $D$  is the diffusivity constant, and  $t$  is the time (Figure 3). The diffusivity constants for the three swarms have low values of  $\sim 0.006$  to  $\sim 0.015$   $\text{m}^2/\text{s}$ , consistent with low-permeability rocks, and have varying diffusivity to the north or south. The focal depth distribution of the 2016–2018 swarm exhibits similar diffusivity rates.

The overall space-time seismicity trends in Figure 3 also exhibit short-term successive surges in the rate of seismicity, suggesting that shorter-time constants may contribute to the overall temporal evolution and cause higher diffusivity during short periods of time. However, resolving such temporal anomalies is difficult.

### 3.5. Fluid Pore Pressure

We use the friction angle between the trend of  $S_{H\text{max}}$  (also called  $\sigma_1$ ) and the average strike of the epicentral distribution of each swarm to determine the likely range of fluid pore pressures (Leclère et al., 2012; Sibson, 1985).

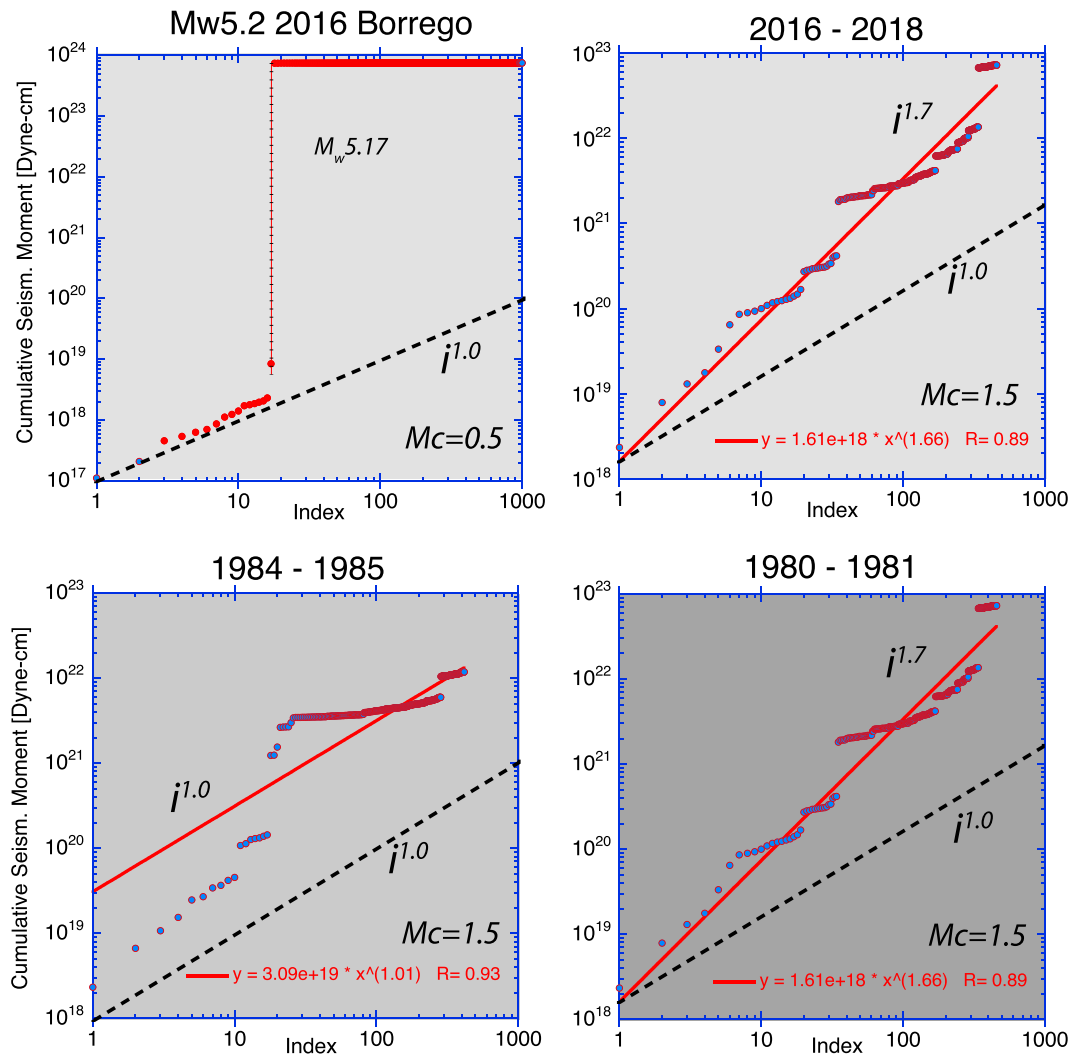


**Figure 9.** Cumulative seismic moment release versus event index for the 2016  $M_w$  5.2 Borrego aftershock sequence and the three Cahuilla swarms. The slope of  $i^{1.0}$  is indicative of time-independent moment release. The steeper slopes suggest a larger rate of moment release with successive events, which can be interpreted as concurrent frequent ruptures on subparallel surfaces.

Assuming that the Coulomb failure criterion applies, and no fault cohesion, Sibson (1985) showed that activating slip on a fault depends on the following: the relative angle between  $\sigma_1$  and the fault plane, the coefficient of static friction, and the pore fluid pressure at the depth of faulting (Leclère et al., 2012). To determine if the stress on a fault was sufficient to cause slip on a fault, Sibson (1985) derived the following formula to determine the conditions of fault reactivation:

$$R = \frac{\sigma_1 - p_f}{\sigma_3 - p_f} = \frac{1 + \mu_s \cot(\theta)}{1 + \mu_s \tan(\theta)}$$

where  $R$  is the effective stress ratio;  $\sigma_1$  and  $\sigma_3$  are the maximum and minimum principal stresses, respectively;  $p_f$  is pore fluid pressure;  $\mu_s$  is the coefficient of static friction on the slip surface; and  $\theta$  is the friction angle between the fault surface and  $\sigma_1$ . Sibson (1985) plotted  $R$  versus  $\theta$  to identify the conditions for which faulting was favorable or unfavorable. In the range of  $10^\circ < \theta < 43^\circ$  the value of  $R$  required is less than 1.5 times the minimum value of  $R$  (Figure 10). In the unfavorable oriented range of  $\theta$  an unrealistically large  $R$  value is required.

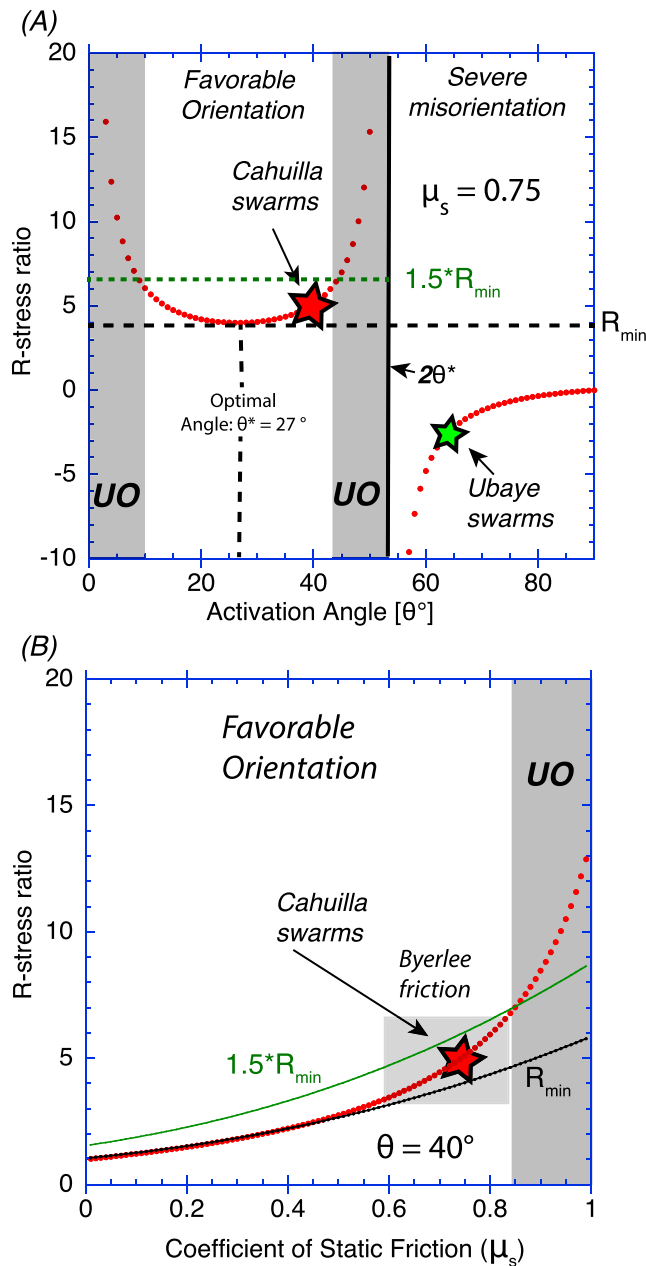


**Figure 10.** (a) The effective stress ratio ( $R$ ) versus the activation angle,  $\theta$ , calculated for a mean coefficient of friction of 0.75. The activation angles from  $10^\circ$  to  $43^\circ$  have favorable orientations for faulting, while activation angles  $<10^\circ$  or  $>43^\circ$  range from unfavorably oriented (UO) to severely misoriented (Sibson, 1985).  $R_{\min}$  corresponds to the optimal angle of faulting, while the  $1.5 * R_{\min}$  is selected as the boundary between favorably and unfavorably oriented faults. The red star represents the Cahuilla swarm with  $\theta = 40^\circ$ , which is in the upper end of the favorable range. The Ubaye, southwestern France-Italian Alps, swarm data are from Leclère et al. (2012). (b) The effective stress ratio ( $R$ ) versus the coefficient of static friction ( $\mu_s$ ) for an activation (faulting) angle of  $\theta = 40^\circ$ . The Cahuilla swarm fits within the Byerlee friction range of  $0.6 < \mu_s < 0.85$ . Also, see Leclère et al. (2012) for comparison with the Ubaye swarm.

Sibson (1985) showed that  $R$  has a minimum positive value of  $R_{\min} = (\sqrt{1 + \mu_s^2} + \mu_s)^2$  at the optimum angle for fault reactivation. This minimum is flat around the optimal  $\theta$  value, but  $R$  approaches two singularities at  $1.5 * R_{\min}$  where the faults are unfavorably oriented (Leclère et al., 2012). We select a coefficient of friction of 0.75, which is appropriate for intact rock and consistent with Byerlee's friction in the range of 0.6 to 0.85 (Leclère et al., 2012). If a smaller  $\mu_s$  value is selected, the required stress ratio becomes smaller but the angle of reactivation does not change significantly. In Figure 10 we apply Sibson's formula to show how the effective stress ratio varies as a function of the activation angle and the coefficient of friction.

The optimal activation angle is  $27^\circ$ , while the friction angle for the Cahuilla swarms is  $\sim 13^\circ$  larger, suggesting that only somewhat elevated pore pressure and minimal cohesion are probably present to accommodate the faulting.

In contrast, a swarm in a granitic terrane of the French-Italian Alps was reported to have a larger friction angle of  $\theta = 63^\circ$  by Leclère et al. (2012). Using a pore fluid factor-differential stress diagram method by Cox (2010), they inferred that an excessive water pressure in the range of 7 to 26 MPa was needed to activate faulting at such unfavorable stress state. In comparison, the angle difference for the Cahuilla swarms is about one third, suggesting elevated pore pressures by 2 to 8 MPa. Thus, there is no need for permeability barriers in the Cahuilla region to explain the seismicity, which are often invoked to explain the presence of high pore pressures. Such layers are sometimes thought to sustain cyclical accumulation of overpressure in addition to slow long-term stress loading (Sibson, 2014).

## 4. Discussion

There are several properties that the Cahuilla earthquake swarms have in common with typical swarms, while other properties are unusual or may be absent. The expected properties include the following: the spatial-temporal evolution of these swarms in a limited depth range, the absence of mainshocks, and the relatively high seismicity rate. The unusual properties consist of their location within the Cahuilla Valley pluton, significantly extended duration, very long range temporal clustering, the absence of variations in  $b$  values with time, and the nonlinear increase in seismic moment rate with time. The absence of geodetic data anomalies and the lack of a mapped late Quaternary throughgoing fault system are also unusual and noteworthy (Morton et al., 2014).

The lack of mainshocks in the two early-1980s swarms as well as in the ongoing (2016 to present) Cahuilla swarm activity suggests that the small-earthquake stress release in the region so far is incomplete. Presence of tectonic intrablock strain loading, pore fluids at depth, and discontinuous fractures with low permeability at low effective stress could explain the extended temporal distribution of the seismicity as well as continued activity in the latest swarm.

### 4.1. Characteristics of the Swarms

The spatial-temporal evolution of the Cahuilla swarms differ from average aftershock sequences in Southern California, which reach a maximum length within hours and do not subsequently expand (Helmstetter et al., 2003). The gradual spatial spreading of these swarms is slow, and

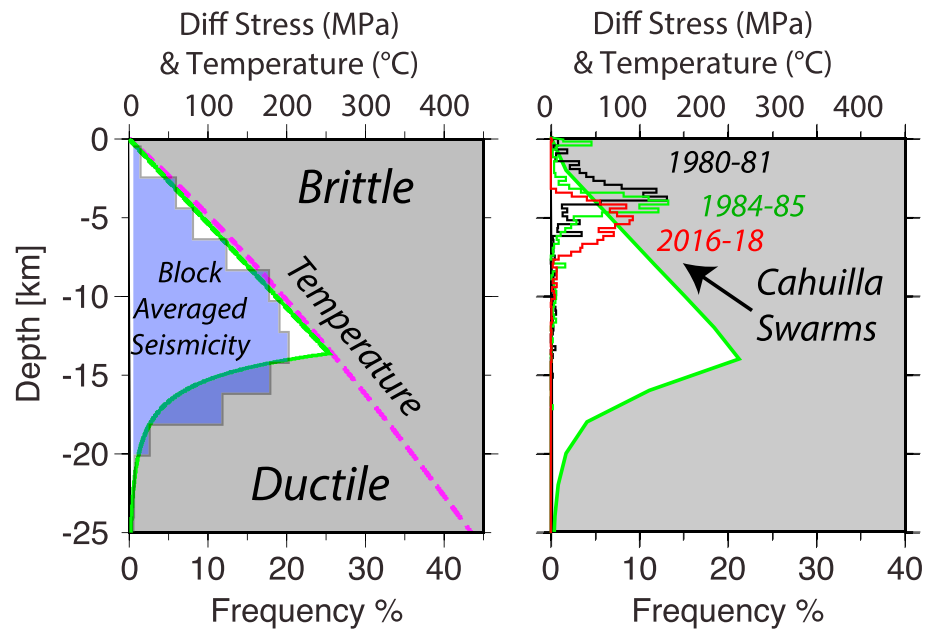


**Figure 11.** Crustal strength profiles showing differential stress and temperature profiles as a function of depth; from Hauksson and Meier (2018). (left) The depth histogram for (1981–2017) seismicity recorded within the east Peninsular Ranges block. (right) The depth histograms for the three Cahuilla swarms color coded with 1980–1981 (black), 1984–1985 (green), and 2016–2018 (red). Note the comparatively shallow depth distributions for the swarms.

if we assume the rate of growth is driven by fluid pressure changes, it is consistent with the low permeability of the plutonic rocks of the Peninsular Ranges. At higher spatial resolution, bursts of seismicity, including some embedded mainshock-aftershock sequences, are superimposed on the overall spatial-temporal migration.

The predominant focal depth range, from ~2 to ~7 km, suggests that these ruptures do not extend through the seismogenic part of the brittle crust (Figure 11). The crust may simply be too cold and strong at depths below 8 km to accommodate seismicity as discussed by Hauksson and Meier (2018) who analyzed seismicity to constrain the strength of the crust. Similarly, the shallow depth of seismicity within a crustal block could be explained by lower and more diffuse strain rate and stress levels away from the main plate boundary faults. In this case, the depth of earthquakes is limited to regions of the crust where the shear stress exceeds the failure strength (Miller & Furlong, 1988).

The Cahuilla swarms have small overall moment release compared to  $M > 5$  mainshock-aftershock sequences that occur about every 6 years in the map area shown in Figure 1. However, the rate of small events is high, in part because it is easy to detect these events in the low attenuation of the batholith and absence of cultural noise sources. The fractal temporal clustering of these abundant swarm events is consistent with a critical failure stress field. In such a stress field, the occurrence of small events may trigger future events (Hainzl & Fischer, 2002). In particular, the power law increase of the average seismic moment release suggests that more than one fault surface is participating in the seismic moment release consistent with the findings of Hainzl (2004).

The ongoing activity in the 2016–2018 swarm supports the idea that the stress release so far is incomplete and the latest swarm will continue. The two most likely future evolution paths for the 2016–2018 swarm are as follows: (1) it continues at the present activity rate for months but slowly decays or (2) it culminates with a larger event in the  $M 5$  range and evolves into a typical decaying aftershock sequence.

#### 4.2. Implications of Invariant $b$ Values

The  $b$  values of the Cahuilla swarms appear to be invariant with time and similar to average values for Southern California (Figures 7 and 8). This observation differs from the observations by Hainzl and Fischer (2002) who reported a  $b$  value decrease as the Vogtland swarms progressed. They interpreted the

decreasing  $b$  value and the nonlinear seismic moment release to indicate that the swarms occurred on a single fault surface driven by one source of pore fluids. In a volcanic study, Shelly et al. (2016) analyzed  $b$  values for high-diffusivity ( $2 \text{ m}^2/\text{s}$ ) swarms in Mammoth Lakes and argued that during periods with low  $b$  values a single fault surface was fault activated, while high  $b$  values were associated with seismicity across several faults.

The Cahuilla swarms exhibited clear strike-slip faulting on a north-south population of joints or foliations that lengthened with time. Migration of activity may be modulated by changes in pore fluid pressure and associated reduction in grain cohesion or could indicate the creation of new fault surfaces. The growth of these surfaces and constant temporal  $b$  values of the Cahuilla swarms may be related to a precarious balance between tectonic loading, limited pore fluid supply, and Coulomb stress triggering interactions between swarm events.

### 4.3. Absence of Geodetic Signals

The absence of a measured geodetic anomaly makes it difficult to associate the Cahuilla swarms with aseismic slip in the epicentral region (Y. Fialko, personal communication, 2018). The most prominent Southern California slow-slip anomaly that was associated with a short-lived swarm occurred near the southern end of the Salton Sea (Lohman & McGuire, 2007). They modeled geodetic data recorded during the 2005 Obsidian Buttes swarm at the south end of the Salton Sea and inferred the occurrence of a shallow aseismic slip event above the seismicity. The migration velocity of 0.1–1.0 km/hr that was observed in the Salton Trough area is fast compared to the Cahuilla swarm migration speeds of 1 to 2 km/year. If there are geodetic signals occurring here, they are too small, or strain accumulation is perhaps too slow, to be detected.

### 4.4. Comparison With Other Earthquake Swarms

Previously similar earthquake swarms in granitic terranes have been reported at locations in other continents. Pytharouli et al. (2011) analyzed induced seismicity located in Brazilian Archean gneisses and Neoproterozoic granites to illuminate fractures extending down to depths of  $\sim 2$  to  $\sim 3$  km. They suggested that the seismicity was being accommodated by movement on an up to 400-m-wide young fracture zone related to mechanical contrast between different geological material exposed by erosional processes. In contrast, the protofault damage zone appeared to remain inactive. They inferred that the first event opened a pathway for a pressure pulse, which in turn triggered the subsequent activity. They analyzed time-distance migration of the swarm and estimated average permeability associated with long open fractures to be  $10^{-15}$  to  $10^{-17} \text{ m}^2$ .

A similar prolific earthquake swarm occurred in the batholithic rocks of the Ubaye Valley, French-Italian Alps, from 2003 to 2004. This swarm consisted of more than 16,000 events in the magnitude range of  $-1.3$  to  $2.7$  with low-diffusivity values of  $\sim 0.05 \text{ m}^2/\text{s}$  (Jenatton et al., 2007). Using more precise hypocenter relocations, Daniel (2011) interpreted the space-time migration of the Ubaye swarm as being caused by diffusion of fluid overpressure of  $< 8 \text{ MPa}$  within the crystalline basement. Applying a formal stress inversion, Leclère et al. (2012) showed that the friction angle for the Ubaye swarm was  $63^\circ$ , which required high overpressures confined by hydraulic barriers. To explain the more than 2-year duration of the swarm, Jenatton et al. (2007) speculated that stress transfer and fluid circulation were in a careful balance enabling the swarm to continue for a long time. The Ubaye and 2016–2018 Cahuilla swarms are very similar in the space-time behavior and geological setting, but the friction angle for the Cahuilla swarm is closer to optimum, and it is probably driven by smaller excess fluid pressures. The tectonic stress loading of the Perris block may provide the extra loading needed to maintain the lower friction angle of  $40^\circ$ .

Previously, Hauksson et al. (2016) studied a swarm located at 12- to 13-km depth beneath the sediments of the Ventura basement in California and found diffusivity values of 20 to 30 times faster than at Cahuilla. Similarly, using seismicity data collected near the German Continental Deep Drilling Borehole (KTB), Shapiro et al. (1997) found higher hydraulic diffusivity of  $\sim 1 \text{ m}^2/\text{s}$  at 7.5- to 9-km depth. Analyzing data from an earthquake swarm in Greece, Duverger et al. (2015) found several hydraulic diffusivity values ranging from about 0.01 to  $0.5 \text{ m}^2/\text{s}$  in a highly fractured layer (probably the phyllite-quartzite nappe) at  $\sim 7$ -km depth. In an unusual case, Malagnini et al. (2012) found diffusivity values around  $50 \text{ m}^2/\text{s}$  for the 2009 L'Aquila earthquake sequence. In a laboratory study, Song and Renner (2007) measured hydraulic diffusivity in sandstone. For sandstone with 8% porosity they found diffusivity of 1 to  $2 \text{ m}^2/\text{s}$ . Rock samples with 5%

porosity had diffusivity of  $\sim 6 \times 10^{-6}$  and  $\sim 7 \times 10^{-5}$  m<sup>2</sup>/s, which is representative of the bulk rock. In a different laboratory study, Wibberley (2002) found hydraulic diffusivity of fine fault zone clay gouge around  $10^{-7}$  (m<sup>2</sup>/s). This wide range in diffusivity values suggests different permeability values, rock composition, and loading stresses. The estimated diffusivity of the Cahuilla swarms that is at the low end of the range measured from seismicity (but still higher than bulk laboratory values) is consistent with the plutonic rocks, which presumably have very low intrinsic permeability values of  $\sim 5 \times 10^{-17}$  m<sup>2</sup>. The Cahuilla swarms may be near the lower boundary for pore fluid-triggered seismicity (Talwani et al., 2007).

Regional geological studies by Morton et al. (2014) identified foliations or joints within the plutonic rock in the area of the swarms. However, there is no evidence for a well-developed late Quaternary fault with a gouge zone. The limited spatial extent of the foliations or joints that likely are accommodating the seismic slip, the lack of a throughgoing fault, and the lack of conjugate foliations (Morton et al., 2014) may explain the very low permeability (and diffusivity) and the limited depth distribution of the swarm events. Because foliations by their nature are spatially heterogeneous and sometimes sealed, they can cause heterogeneity of pore fluid pressures, which may result in earthquake-driven fault-valve behavior (Sibson, 2007). In a different study, Zaliapin and Ben-Zion (2013) identified swarm-like clusters and associated them with mixed brittle-ductile failures in regions of high temperature or fluid content. Both the temperature and permeability of the crust in the Peninsular Ranges are relatively low, demonstrating that small quantities of fluids at average crustal temperatures can also cause earthquake swarms of extended duration.

## 5. Conclusions

In this paper, we synthesize data from three Cahuilla Valley earthquake swarms that occurred in 1980–1981, 1983–1984, and 2016–2018 within the Cahuilla Valley pluton of the batholithic terrane of the Peninsular Ranges of Southern California. The cause of the Cahuilla swarms is most likely a combination of intrablock plate tectonic stress loading and presence of pore fluids along favorably oriented weak joints or foliations embedded within a strong rock matrix. These swarms are located halfway between the San Jacinto and Elsinore faults and thus do not accommodate significant plate motion and may not be affecting either fault with stressing rate changes.

The lack of mainshocks, abundance of small events, and clear spatial-temporal migration is consistent with pore fluid-driven swarms and Coulomb-type stress interaction between events. The overall slow migration velocities and very long duration are to be expected for low strain rates and very low permeability. The absence of a late Quaternary fault zone and geodetic anomalies, as well as very low permeability, and limited depth distribution suggest that these may be reactivated joints or foliations in the plutonic rock. In addition, regional spatial heterogeneity in rock composition and possibly slightly enhanced pore fluid pressures ( $\sim 2$  to  $\sim 5$  MPa) may influence the details of the features of the three swarms such as geographical location, total duration, the speed of onset, and depth distributions.

The earthquake hazards implications of the 2016–2018 Cahuilla swarm zone of seismic slip are minimal as compared to the nearby major players, the San Andreas, San Jacinto, and Elsinore faults. In part these earthquakes are limited in size because the swarm zone only penetrates about halfway to the base of the seismogenic zone and because both the stress level and strain rate are too low to counteract the strength of the plutonic rocks. The absence of large events ( $M > 5$ ) and ongoing activity across the 2016–2018 swarm zone supports the idea that the stress release so far is incomplete and the 2016–2018 swarm will continue possibly for months.

## References

- Båth, M. (1965). Lateral inhomogeneities of the upper mantle. *Tectonophysics*, *2*(6), 483–514. [https://doi.org/10.1016/0040-1951\(65\)90003-X](https://doi.org/10.1016/0040-1951(65)90003-X)
- Cox, S. F. (2010). The application of failure mode diagrams for exploring the roles of fluid pressure and stress states in controlling styles of fracture-controlled permeability enhancement faults and shear zones. *Geofluids*, *10*, 217–233.
- Daniel, G. (2011). Changes in effective stress during the 2003–2004 Ubaye seismic swarm, France. *Journal of Geophysical Research*, *116*, B01309. <https://doi.org/10.1029/2010JB007551>
- Duverger, C., Godano, M., Bernard, P., Lyon-Caen, H., & Lambotte, S. (2015). The 2003–2004 seismic swarm in the western Corinth rift: Evidence for a multiscale pore pressure diffusion process along a permeable fault system. *Geophysical Research Letters*, *42*, 7374–7382. <https://doi.org/10.1002/2015GL065298>

### Acknowledgments

We thank L. M. Jones, M-A Meier, and J. Stock for discussions and R. Graves, K. Scharer, and D. Kilb for comprehensive reviews. This research was supported by USGS/NEHRP grants G16AP00147 and G18AP00028; by NSF awards EAR-1550704 and EAR-1818582; and by the Southern California Earthquake Center (contribution no. 9027). SCEC is funded by NSF Cooperative Agreement EAR-1600087 and USGS Cooperative Agreement G17AC00047. We used GMT from Wessel et al. (2013) to make the figures. We have used waveforms and parametric data from the Caltech/USGS Southern California Seismic Network (SCSN), doi: 10.7914/SN/CI, stored at the Southern California Earthquake Data Center. doi:10.7909/C3WD3xH1. There are no real or perceived financial conflicts of interests for any author.

- Hainzl, S. (2004). Seismicity patterns of earthquake swarms due to fluid intrusion and stress triggering. *Geophysical Journal International*, 159(3), 1090–1096. <https://doi.org/10.1111/j.1365-246X.2004.02463.x>
- Hainzl, S., & Fischer, T. (2002). Indications for a successively triggered rupture growth underlying the 2000 earthquake swarm in Vogtland/NW Bohemia. *Journal of Geophysical Research*, 107(B12), 2338. <https://doi.org/10.1029/2002JB001865>
- Hainzl, S., Scherbaum, F., & Beauval, C. (2006). Estimating background activity based on interevent-time distribution. *Bulletin of the Seismological Society of America*, 96(1), 313–320. <https://doi.org/10.1785/0120050053>
- Hardebeck, J. L., & Shearer, P. M. (2003). Using *S/P* amplitude ratios to constrain the focal mechanisms of small earthquakes. *Bulletin of the Seismological Society of America*, 93(6), 2434–2444. <https://doi.org/10.1785/0120020236>
- Hauksson, E. (2000). Crustal structure and seismicity distributions adjacent to the Pacific and North America plate boundary in southern California. *Journal of Geophysical Research*, 105(B6), 13,875–13,903. <https://doi.org/10.1029/2000JB900016>
- Hauksson, E., Andrews, J., Plesch, A., Shaw, J. H., & Shelly, D. R. (2016). The 2015 earthquake swarm near Fillmore, California: Possible dehydration event near the bottom of the over-pressurized Ventura Basin. *Seismological Research Letters*, 87(4), 807–815. <https://doi.org/10.1785/0220160020>
- Hauksson, E., & Meier, M.-A. (2018). Applying depth distribution of seismicity to determine thermo-mechanical properties of the seismogenic crust in southern California: Comparing lithotectonic blocks. *Pure and Applied Geophysics* Retrieved from, 176(3), 1061–1081. <https://doi.org/10.1007/s00024-018-1981-z>
- Hauksson, E., & Shearer, P. (2006). Attenuation models ( $Q_P$  and  $Q_S$ ) in three-dimensions of the southern California crust: Inferred fluid saturation at seismogenic depths. *Journal of Geophysical Research*, 111, B05302. <https://doi.org/10.1029/2005JB003947>
- Hauksson, E., Shearer, P. M., & Yang, W. (2012). Waveform relocated earthquake catalog for southern California (1981 to June 2011). *Bulletin of the Seismological Society of America*, 102(5), 2239–2244. <https://doi.org/10.1785/0120120010>
- Helmstetter, A., Ouillon, G., & Sornette, D. (2003). Are aftershocks of large Californian earthquakes diffusing? *Journal of Geophysical Research*, 108(B10), 2483. <https://doi.org/10.1029/2003JB002503>
- Hutton, L. K., Woessner, J., & Hauksson, E. (2010). Seventy-seven years (1932–2009) of earthquake monitoring in southern California. *Bulletin of the Seismological Society of America*, 100(2), 423–446. <https://doi.org/10.1785/0120090130>
- Jenatton, L., Guiguet, R., Thouvenot, F., & Daix, N. (2007). The 16,000-event 2003–2004 earthquake swarm in Ubaye (French Alps). *Journal of Geophysical Research*, 112, B11304. <https://doi.org/10.1029/2006JB004878>
- Jennings, C. W., & Bryant, W. A. (2010). Fault activity map of California. Geologic Data Map No. 6, California Geological Survey. Retrieved from <http://maps.conservation.ca.gov/cgs/fam/>
- Koper, K. D., Pankow, K. L., Pechmann, J. C., Hale, J. M., Burlacu, R., & Yeck, W. L. (2018). Afterslip enhanced aftershock activity during the 2017 earthquake sequence near Sulphur Peak, Idaho. *Geophysical Research Letters*, 45, 5352–5361. <https://doi.org/10.1029/2018GL078196>
- Leclère, H., Fabbri, O., Daniel, G., & Cappa, F. (2012). Reactivation of a strike-slip fault by fluid overpressuring in the southwestern French-Italian Alps. *Geophysical Journal International*, 189(1), 29–37. <https://doi.org/10.1111/j.1365-246X.2011.05345.x>
- Lindsey, E. O., & Fialko, Y. (2013). Geodetic slip rates in the southern San Andreas Fault system: Effects of elastic heterogeneity and fault geometry. *Journal of Geophysical Research: Solid Earth*, 118, 689–697. <https://doi.org/10.1029/2012JB009358>
- Lohman, R. B., & McGuire, J. J. (2007). Earthquake swarms driven by aseismic creep in the Salton Trough, California. *Journal of Geophysical Research*, 112, B04405. <https://doi.org/10.1029/2006JB004596>
- Malagnini, L., Lucente, F. P., Gori, P. D., Akinci, A., & Munafò, I. (2012). Control of pore fluid pressure diffusion on fault failure mode: Insights from the 2009 L'Aquila seismic sequence. *Journal of Geophysical Research*, 117, B05302. <https://doi.org/10.1029/2011JB008911>
- Matoza, R., Shearer, P. M., Lin, G., Wolfe, C., & Okubo, P. (2013). Systematic relocation of seismicity on Hawaii Island from 1992 to 2009 using waveform cross-correlation and cluster analysis. *Journal of Geophysical Research: Solid Earth*, 118, 2275–2288. <https://doi.org/10.1002/jgrb.50189>
- Michael, A. J. (1984). Determination of stress from slip data: Faults and folds. *Journal of Geophysical Research*, 89(B13), 11,517–11,526. <https://doi.org/10.1029/JB089B13p11517>
- Miller, C. K., & Furlong, K. P. (1988). Thermal-mechanical controls on seismicity depth distributions in the San Andreas Fault Zone. *Geophysical Research Letters*, 15(12), 1429–1432. <https://doi.org/10.1029/GL015i012p01429>
- Morton, D. M., Miller, F. K., Kistler, R. W., Premo, W. R., Lee, C.-T. A., Langenheim, V. E., & Cossette, P. (2014). Framework and petrogenesis of the northern Peninsular Ranges batholith, southern California. In D. M. Morton, & F. K. Miller (Eds.), *Peninsular Ranges batholith, Baja California and southern California, Geological Society of America Memoir* (Vol. 211, pp. 61–143). [https://doi.org/10.1130/2014.1211\(03\)](https://doi.org/10.1130/2014.1211(03))
- Pytharoulis, S. I., Lunn, R. J., Shipton, Z. K., Kirkpatrick, J. D., & do Nascimento, A. F. (2011). Microseismicity illuminates open fractures in the shallow crust. *Geophysical Research Letters*, 38, L02402. <https://doi.org/10.1029/2010GL045875>
- Ross, Z. E., Hauksson, E., & Ben-Zion, Y. (2017). Abundant off-fault seismicity and orthogonal structures in the San Jacinto fault zone. *Science Advanced*, 3(3), e1601946. <https://doi.org/10.1126/sciadv.1601946>
- Ruhl, C. J., Abercrombie, R. E., Smith, K. D., & Zaliapin, I. (2016). Complex spatiotemporal evolution of the 2008  $M_w$  4.9 Mogul earthquake swarm. *Journal of Geophysical Research: Solid Earth*, 121, 8196–8216. <https://doi.org/10.1002/2016JB013399>
- Shapiro, S. A., Huenges, E., & Borm, G. (1997). Estimating the crust permeability from fluid-injection-induced seismic emission at the KTB site. *Geophysical Journal International*, 131(2), F15–F18. <https://doi.org/10.1111/j.1365-246X.1997.tb01215.x>
- Shearer, P. M., Prieto, G. A., & Hauksson, E. (2006). Comprehensive analysis of earthquake source spectra in southern California. *Journal of Geophysical Research*, 111, B06303. <https://doi.org/10.1029/2005JB003979>
- Shelly, D. R., Ellsworth, W. L., & Hill, D. P. (2016). Fluid-faulting evolution in high definition: Connecting fault structure and frequency-magnitude variations during the 2014. *Journal of Geophysical Research: Solid Earth*, 121, 1776–1795. <https://doi.org/10.1002/2015JB012719>
- Sibson, R. H. (1985). A note on fault reactivation. *Journal of Structural Geology*, 7–75.
- Sibson, R. H. (2007). An episode of fault-valve behaviour during compressional inversion?—The 2004 MJ6.8 Mid-Niigata Prefecture, Japan, earthquake sequence. *Earth and Planetary Science Letters*, 257(1–2), 188–199. <https://doi.org/10.1016/j.epsl.2007.02.031>
- Sibson, R. H. (2014). Earthquake rupturing in fluid-overpressured crust: How common? *Pure and Applied Geophysics*, 171(11), 2867–2885. <https://doi.org/10.1007/s00024-014-0838-3>
- Song, I., & Renner, J. (2007). Analysis of oscillatory fluid flow through rock samples. *Geophysical Journal International*, 170(1), 195–204. <https://doi.org/10.1111/j.1365-246X.2007.03339.x>
- Talwani, P., Chen, L., & Gahalaut, K. (2007). Seismogenic permeability,  $k_s$ . *Journal of Geophysical Research*, 112, B07309. <https://doi.org/10.1029/2006JB004665>

- Touati, S., Naylor, M., & Main, I. G. (2009). Origin and nonuniversality of the earthquake interevent time distribution. *Physical Review Letters*, *102*(16), 168501. <https://doi.org/10.1103/PhysRevLett.102.168501>
- Vidale, J. E., & Shearer, P. M. (2006). A survey of 71 earthquake bursts across southern California: Exploring the role of pore fluid pressure fluctuations and aseismic slip as drivers. *Journal of Geophysical Research*, *111*, B05312. <https://doi.org/10.1029/2005JB004034>
- Wells, D. L., & Coppersmith, K. J. (1994). New empirical relationships among magnitude, rupture length, rupture width, rupture area and surface displacement. *Bulletin of the Seismological Society of America*, *84*(4), 974–1002.
- Wessel, P., Smith, W. H. F., Scharroo, R., Luis, J. F., & Wobbe, F. (2013). Generic Mapping Tools: Improved version released. *Eos, Transactions American Geophysical Union*, *94*(45), 409–410. <https://doi.org/10.1002/2013EO450001>
- Wibberley, C. A. J. (2002). Hydraulic diffusivity of fault gouge zones and implications for thermal pressurization during seismic slip. *Earth, Planets and Space*, *54*(11), 1153–1171. <https://doi.org/10.1186/BF03353317>
- Wiemer, S. (2001). A software package to analyze seismicity: ZMAP. *Seismological Research Letters*, *72*(3), 373–382. <https://doi.org/10.1785/gssrl.72.3.373>
- Yang, W., & Hauksson, E. (2013). The tectonic crustal stress field and style of faulting along the Pacific North America plate boundary in southern California. *Geophysical Journal International*, *194*(1), 100–117. <https://doi.org/10.1093/gji/ggt113>
- Yang, W., Hauksson, E., & Shearer, P. (2012). Computing a large refined catalog of focal mechanisms for southern California (1981–2010): Temporal stability of the style of faulting. *Bulletin of the Seismological Society of America*, *102*(3), 1179–1194. <https://doi.org/10.1785/0120110311>
- Zaliapin, I., & Ben-Zion, Y. (2013). Earthquake clusters in southern California I: Identification and stability. *Journal of Geophysical Research: Solid Earth*, *118*, 2847–2864. <https://doi.org/10.1002/jgrb.50179>